Global spherical harmonic models of the internal magnetic field of the Moon based on sequential and coestimation approaches

Michael E. Purucker[1] and Joseph B. Nicholas[1]

Received 13 May 2010; revised 19 July 2010; accepted 20 August 2010; published 10 December 2010.

[1] Three new models of the global internal magnetic field of the Moon based on Lunar Prospector (LP) fluxgate magnetometer observations are developed for use in understanding the origin of the Moon's crustal magnetic field and for modeling its interaction with the solar wind. The models are at spherical harmonic degree 170, corresponding to 64 km wavelength resolution, from 30 km mean altitude LP observations. Coverage is complete except for a few areas near each pole. Original signal amplitudes are best preserved in the sequential approach map, whereas feature recognition is superior in the coestimation and harmonic wave number correlation maps. Spherical harmonic degrees less than 15, corresponding to 666 km wavelength, are largely absent from the Moon's internal magnetic field. We interpret this bound in terms of the Moon's impact history. A derived magnetization map suggests magnetizations may locally exceed 0.2 A/m in the lunar crust at the survey resolution if the magnetic crust is as thick as 40 km.

Citation: Purucker, M. E., and J. B. Nicholas (2010), Global spherical harmonic models of the internal magnetic field of the Moon based on sequential and coestimation approaches, *J. Geophys. Res.*, *115*, E12007, doi:10.1029/2010JE003650.

1. Introduction

[2] Maps of the internal magnetic field of the Moon find use in deciphering the early history of the Moon, especially whether it possessed a primordial dynamo field [*Fuller*, 1998; *Garrick-Bethell et al.*, 2009]. More generally, we are interested in how these internal fields originate, because the Moon does not possess a dynamo-driven field at present. One candidate for the origin of these fields is as a thermal remanent magnetization (TRM), acquired when the rocks cooled below their Curie temperature. The other leading candidate for the origin of these internal fields is via the amplification of existing fields during large basin-forming impacts [*Hood and Artemieva*, 2008].

[3] Internal magnetic fields at the Moon were first recognized by particles and fields instruments onboard the Apollo 15 and 16 subsatellites. The polar-orbiting Lunar Prospector [*Binder*, 1998] provided the first global mapping of the lunar magnetic field from low (11–66 km) orbit in 1998 and 1999. Both electron reflectometer [*Halekas et al.*, 2001] and triaxial fluxgate magnetometers [*Hood et al.*, 2001] provided mappings. The electron reflectometer employs a remote sensing approach to place bounds on the magnitude of the magnetic field at the surface, while the magnetometer measures the direction and strength of the vector magnetic field at the satellite. Lunar Prospector was followed in 2007 and 2008 by the Japanese Kaguya satellite, which mapped the magnetic fields at an altitude of 100 km and lower, utilizing a triaxial fluxgate magnetometer [*Matsushima et al.*, 2010; *Toyoshima et al.*, 2008; *Shimizu et al.*, 2008; *Takahashi et al.*, 2009].

[4] Previous maps of the magnetic field, based on the missions above, include local, space domain maps [*Tsunakawa et al.*, 2010] and global, spherical harmonic [*Purucker*, 2008] maps to spherical harmonic degree 150. Maps based on the magnetometer data include those of *Richmond and Hood* [2008], while those based on the electron reflectometer data include those of *Mitchell et al.* [2008].

2. Data

[5] The low-noise (6 pT RMS) fluxgate magnetometers on the spin-stabilized Lunar Prospector spacecraft were mounted on a 2.5 m boom in order to minimize spacecraft influences. The spin-averaged measurements of the nominal 18 Hz magnetic field observations are at 5 second intervals, corresponding to an along-track sampling of 9 km. Our analysis first converted the Level 1B data from NASA's Planetary Data System (PDS, UCLA, Particles and Fields node) to a local tangent coordinate system with B_r positive outward, B_θ positive southward, and B_ϕ positive eastward.

[6] Three lunar magnetic regimes are distinguished. The wake regime represents observations made in the lunar wake, when the Sun is obscured by the Moon. The solar wind regime represents observations made when the Sun is visible from the satellite, and out of the Earth's magnetotail. The tail regime represents observations made within the Earth's magnetotail (Figure 1).

[7] A fourth regime represents observations made within the Earth's magnetosheath. This regime is transitional between the tail and wind regimes, and data sampled there

[1]Raytheon at Planetary Geodynamics Laboratory, Goddard Space Flight Center, Greenbelt, Maryland, USA.

Copyright 2010 by the American Geophysical Union.
0148-0227/10/2010JE003650

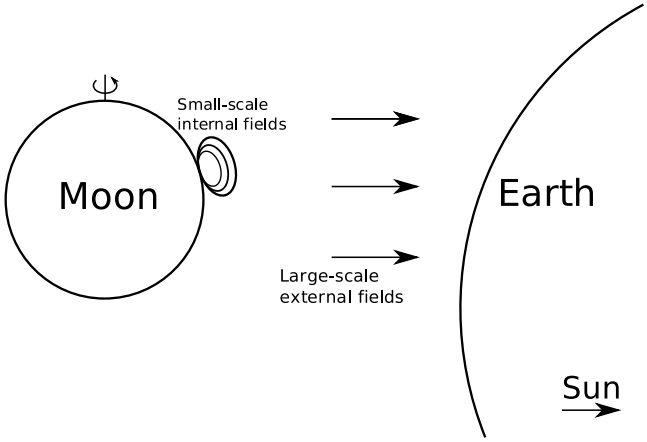

Figure 1. Magnetic fields and model parameterization showing large-scale external magnetic fields and small-scale internal magnetic fields in the vicinity of the Moon. The situation shown here, with magnetic field lines pointing back toward the Earth, has the Moon in the northern lobe of the Earth's magnetosphere. The assumption of steady and uniform external magnetic fields is best met when the moon and Lunar Prospector are in the Earth's magnetosphere. External magnetic fields can be more variable, but are also generally much smaller, in the lunar wake. The most variability and the largest fields are encountered in the solar wind environment. The external magnetic fields are modeled in a selenographic coordinate system, with the z axis along the rotation axis of the Moon, positive in the direction of angular momentum. The x axis lies in the lunar equatorial plane at 0° longitude, and the y axis completes the right-hand coordinate system. Internal magnetic fields are modeled in the usual local tangent coordinate system employed in geomagnetism.

are not included in the final maps made using our procedures. All maps shown here utilize data collected only in the wake and tail regimes. It has been previously shown [*Purucker*, 2008] that maps made using data from solar wind times are compressed and distorted relative to those from wake and tail times.

3. Model Development and Parameterization

[8] Two different parameterizations are used to characterize the internal magnetic field of the Moon. We do this because different parameterizations allow us to emphasize different attributes of the solution, and to determine error limits on the solutions. We first describe our overall philosophy of model development. We then briefly describe the sequential approach, using a line of dipoles to characterize the internal field along a spacecraft track [*Purucker*, 2008]. We next describe, in detail, a coestimation approach, using a harmonic basis to characterize the internal field. We finish up this section by describing the strengths and limitations of these two approaches.

[9] Our philosophy is dictated by the computational problems associated with developing least squares models of large data sets. Even in conjugate gradient approaches [*Purucker et al.*, 1996], the memory requirements go as $O(po)$ where p is the number of parameters and o the number of observations. The least squares models described here have in excess of 32000 parameters, and 2.7 million observations. Instead of trying to develop this large model in 2 dimensions, we develop them in 1 dimension using the along-track and radial components of three adjacent passes collected during a particular lunar regime. As long as the distance between adjacent passes is less than or similar to the distance above the magnetic source, the adjacent passes will be sensitive to common internal magnetic sources. We then extend our models from one to two dimensions using the Driscoll and Healy sampling theorem [*Driscoll and Healy*, 1994].

3.1. Sequential Approach

[10] The external magnetic field in the sequential, line dipole approach is represented as a uniform field over each satellite half orbit (Figure 1), and the half orbits extend from pole to pole. The technique was first described by *Nicholas et al.* [2007] and later by *Purucker* [2008]. The external field was determined in a least squares sense from all three components of the vector data. Following the removal of the external field model from each half orbit, an internal line dipole model is developed in spherical coordinates [*Dyment and Arkani-Hamed*, 1998], utilizing three adjacent half orbits which are separated in space by about 1° (30 km), and in time by 1.9 h. The crust under the three adjacent half orbits is divided into blocks, each of which is assumed to have a magnetic dipole at its center. A horizontal dipole is located under each observation of the center pass, on the 1737.1 km mean lunar radius surface.

[11] The magnetic field is represented as the gradient of a scalar magnetic potential

$$V(r,\theta,\phi) = -\vec{M}\cdot\nabla\left(\frac{1}{l}\right) \tag{1}$$

where $\vec{M}$ is the dipole moment and

$$l = \sqrt{r^2 + r'^2 - 2rr'\cos\zeta} \tag{2}$$

where l is the distance between the source and the dipole and ζ is the angle between r and r'.

[12] $\vec{M}$ is constrained by observations of B_r and B_θ, and in the previous implementation of this approach for the Moon [*Purucker*, 2008] the distance between the source and the dipole for the observations of B_θ was incorrect by a factor of l. This had the effect of decreasing the amplitude of the resulting map of B_r, but did not change the location of the magnetic features, as we will show. As before, we utilized a preconditioned conjugate gradient approach [*Purucker et al.*, 1996], and iterated each solution six times. Each solution, of which there were in excess of 5000 low-altitude ones, was used to calculate the radial magnetic field at an altitude of 30 km above the mean lunar radius. Figure 2 shows the radial magnetic field profiles and grids over the Reiner Gamma swirl [*Nicholas et al.*, 2007], one of the largest isolated magnetic features on the Moon. Figure 3 shows the radial magnetic profiles and grids over the northwestern corner of the South Polar Aitken basin, the location of the most extensive set of magnetic features on the Moon. Profiles and maps before and after the major processing steps are shown, and emphasize the clarification of the

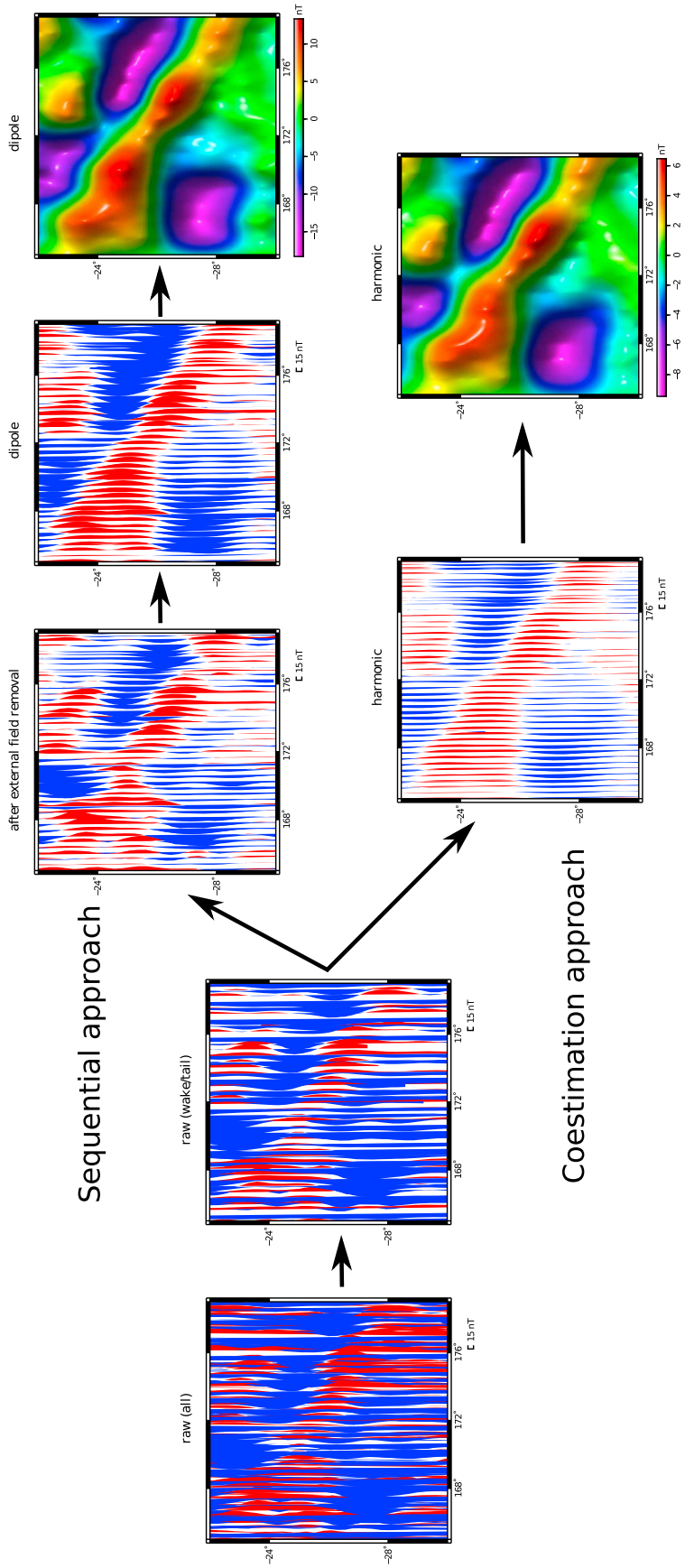

Figure 2. Radial magnetic field processing steps associated with the sequential and coestimation approaches over Reiner Gamma, with the progression shown by arrows connecting the maps. The individual profiles are colored red where the field is positive, blue where the field is negative. The "raw(all)" profile represents the starting point, and includes all low-altitude passes over the feature. The "raw(wake/tail)" profile shows the subset of raw data from wake and tail times. The sequential and coestimation approaches then diverge, and the coestimation approach first removes a uniform external magnetic field from the wake and tail observations. This is shown in the "after external field removal" profile. This is followed by fitting the resulting field to an internal set of dipoles. The profile and gridded views are labeled "dipole." The coestimation approach uses a harmonic basis to coestimate internal and external fields, and the profile and map views are labeled "harmonic." Cylindrical equidistant projections.

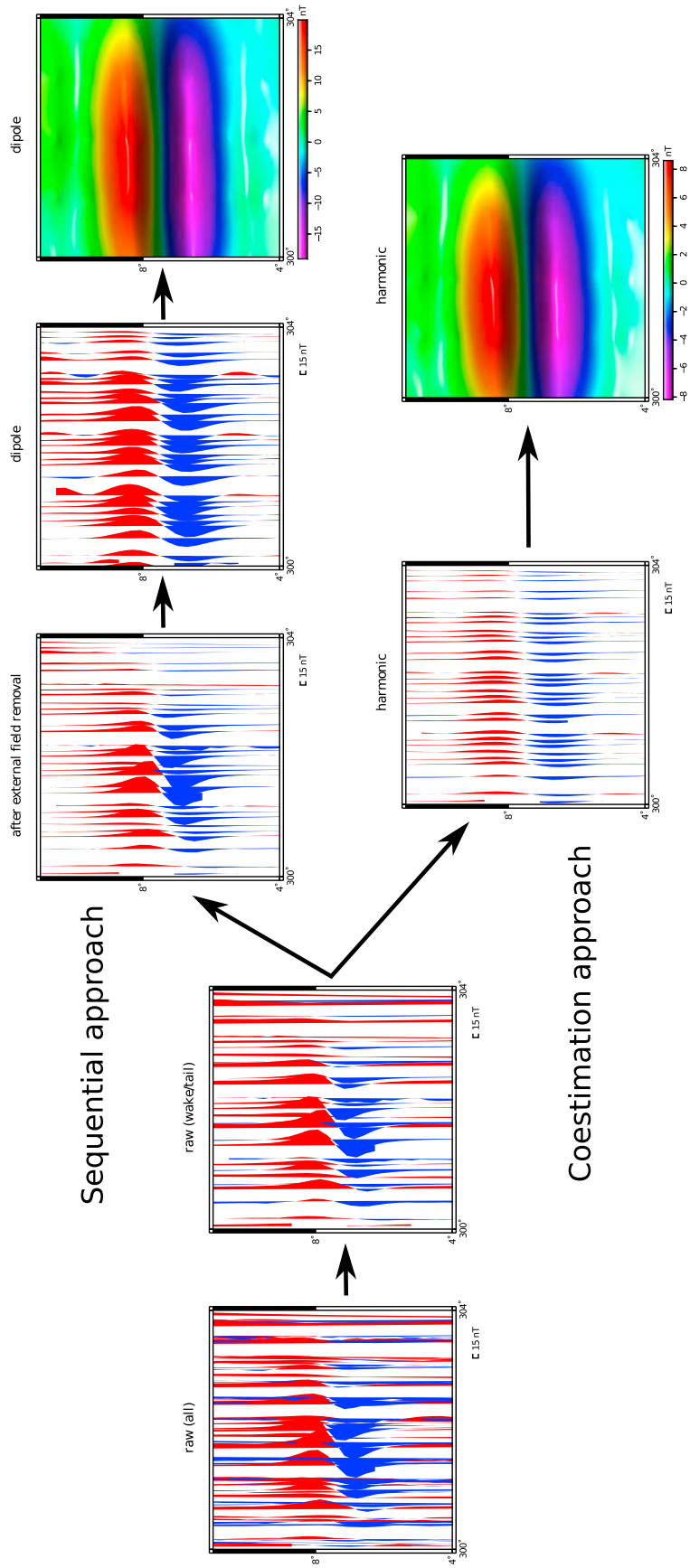

Figure 3. Radial magnetic field processing steps associated with the sequential and coestimation approaches over the South Pole-Aitken basin region, with the progression shown by arrows connecting the maps. See Figure 2 for further details.

features which occurs after each processing step. As can be seen, individual magnetic features are located in the same position in the two approaches, and the major difference seen here is in the difference in the magnitude of the magnetic features. This will be discussed further below.

3.2. Coestimation Approach

[13] The second parameterization utilizes a harmonic approach to characterize the internal magnetic field, and coestimates the internal and external magnetic fields. The external magnetic fields are still described, as in the sequential approach, as a uniform external field over each satellite half orbit (Figure 1).

[14] We again utilize both B_r and B_θ observations to constrain the model, and represent those vectors as the gradient of a scalar magnetic potential

$$B_r = -\frac{\partial V}{\partial r} = \sum_{n=1}^{180}\left[(n+1)g_n^0\left(\frac{a}{r}\right)^{n+2}\right]P_n^0(\theta) \tag{3}$$

$$B_\theta = -\frac{1}{r}\frac{\partial V}{\partial \theta} = -\sum_{n=1}^{180}\left[g_n^0\left(\frac{a}{r}\right)^{n+2}\right]\frac{\mathrm{d}P_n^0(\theta)}{\mathrm{d}\theta} \tag{4}$$

where a is the mean radius of the Moon, P_n^0 are the associated Legendre functions of degree n and order 0, and the g_n^0 are the internal coefficients to be determined from observations of B_r and B_θ at radial distance r from the center of the Moon [*Langel*, 1987]. The resulting fields calculated from the model are continued to an altitude of 30 km. The least squares problem is solved using singular value decomposition. In a variant of this approach, we first demean the individual profiles because of the absence of a monopole term in our solution. We find that this variant approach yields solutions that are almost indistinguishable, in terms of the magnitude and location of the resulting magnetic features, to our standard approach.

3.3. Strengths and Limitations

[15] Coestimating the internal and external magnetic fields allows for an estimate of the covariance of the solution, in contrast to the sequential approach where no such information is available. The correlation between parameters i and j is defined in terms of the Covariance matrix C as

$$\rho_{ij} = \frac{C(i,j)}{\sqrt{C(i,i)C(j,j)}} \tag{5}$$

[16] Analysis of the covariance matrix indicates that the highest correlations, up to 0.24, occur between the external field solution and the lowest-degree internal coefficients. This is to be expected based on our parameterization of the internal and external fields (Figure 1). Correlations decrease to 0.1 by degree 4, and hence we have removed internal degrees 1 through 3 from our final 1-D solutions. The exact cutoff is subjective, and involves an assessment of the tradeoff between improved track leveling, and the decreased amplitude in the final signal. We find that removal of degrees 1 through 3 makes a significant visual improvement to track leveling, while minimizing signal amplitude reduction.

[17] The coestimation approach assumes that the longitude of the three adjacent passes are identical. This limitation of the coestimation approach has the effect of suppressing significantly the amplitude of the anomalies, as can be seen in Figures 2 and 3. This suppression seems to be largest in magnetic features which have east-west extents comparable to the width of the three adjacent passes, or approximately 2°. Reiner Gamma (Figure 2) is an example of such a feature, and we see larger amplitude suppressions here than in the South Polar Aitken region (Figure 3).

[18] Both approaches share some additional limitations. They are not able to incorporate the B_ϕ component into the modeling because B_ϕ is sensitive to the east-west extent of a magnetic source. However, B_ϕ is usually the component most affected by poorly modeled external and toroidal fields, and so neglecting it is justified on these grounds. A more important limitation is that internal magnetic fields parallel to the polar-orbiting LP spacecraft are not as well characterized as those in other directions.

4. From One Dimension to Two Dimensions

[19] The radial magnetic field model data sets resulting from the sequential and coestimation approaches just described are binned into 360 by 360 equiangular bins, 1° in longitude by 1/2° in latitude. Median fields for wake and tail times are then calculated for each bin in order to produce a robust estimate of the field, minimally affected by outliers. More than 99% of the bins were populated for each of the approaches. The unpopulated bins are concentrated in a few areas within 20° of the poles, as shown in Figure 4. The binned data are then fit to a continuous curvature surface [*Wessel and Smith*, 1998] with adjustable tension set to 0.25, appropriate for potential field observations.

5. Spherical Harmonic Models of Magnetic Field and Magnetization

[20] The gridded data sets representing the sequential and coestimation approaches are then utilized to construct spherical harmonic models to degree and order 180 with the Driscoll and Healy sampling theorem [*Driscoll and Healy*, 1994], and shown in Figures 5 and 6, respectively.

[21] The magnetic potential is traditionally represented as

$$V = a\sum_{n=1}^{180}\left(\frac{a}{r}\right)^{n+1}\sum_{m=0}^{n}\left[g_n^m\cos(m\phi) + h_n^m\sin(m\phi)\right]P_n^m(\theta) \tag{6}$$

where θ is colatitude, and ϕ longitude, P_n^m are the Schmidt quasi-normalized associated Legendre functions of degree n and order m, and the g_n^m and h_n^m are the coefficients of the model.

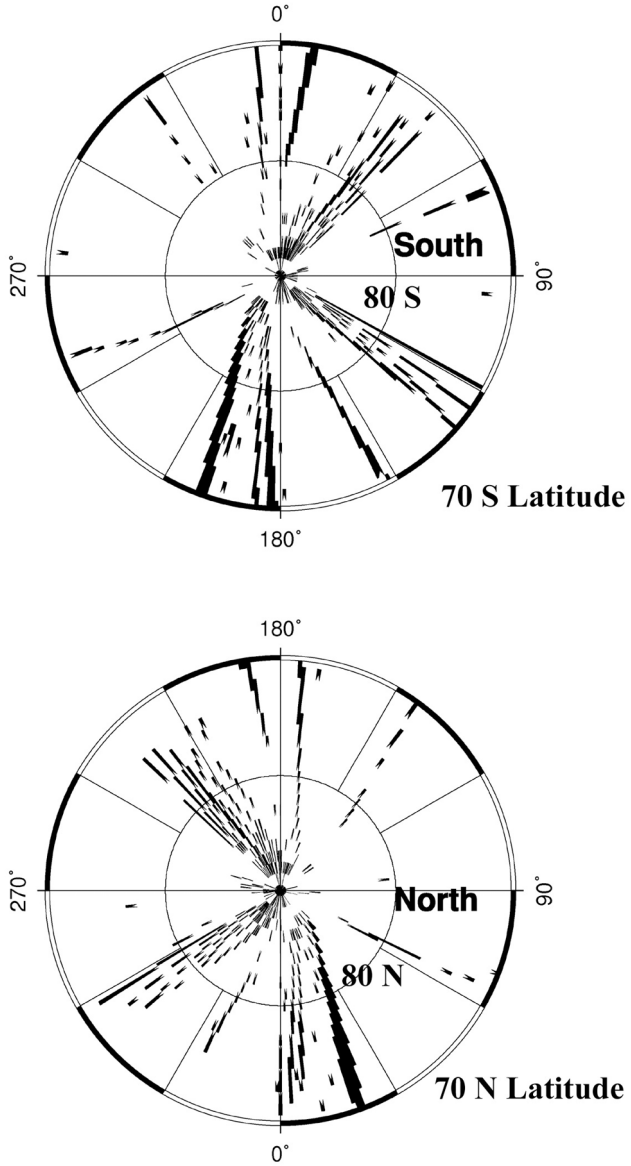

Figure 4. The location of bins in the polar regions (within 20° of the poles) for which we have no observations.

[22] An assessment of the correlation of the two maps can be made in the spherical harmonic domain using degree correlations [*Langel and Hinze*, 1998], defined as

$$\rho_n = \frac{\sum_{m=0}^{n}(g_{nm}g'_{nm} + h_{nm}h'_{nm})}{\sqrt{\left[\sum_{m=0}{}^{n}(g_{nm}{}^2 + h_{nm}{}^2)\right]\left[\sum_{m=0}^{n}(g'^2_{nm} + h'^2_{nm})\right]}} \quad (7)$$

for each degree n.

[23] The degree by degree correlations of these two maps (Figure 7) indicate high correlations between degrees 15 and 170, decreasing slightly at the highest degrees. We present all of our maps between degrees 1 and 170 because degree correlations between our two maps dip below 0.75 at about degree 170. The low correlations between degrees 1 and 14 suggest that users might also wish to omit, or interpret with care, information from those lowest degrees. All of our model coefficients, derived grids and metadata, are available on our Web site at http://core2.gsfc.nasa.gov/research/purucker/moon_2010.

[24] We apply a harmonic wave number correlation technique [*Langel and Hinze*, 1998] to extract common features of the two maps (Figure 8), retaining coefficients from the coestimation map that differ by less than 30% phase angle from their counterparts in the sequential map. This technique is often applied in geomagnetic applications [*Langel and Hinze*, 1998] in order to minimize the influence of noncrustal components in the final map. While emphasizing the common features, it also sometimes reduces the amplitude of the map significantly. In this case, only minimal amplitude reduction was noted from the coestimation map. The choice of phase angle, or equivalently, correlation, is a subjective one but the trade to be assessed is between removing noncorrelative magnetic field components on one hand, and amplitude reduction on the other hand. The phase angle selected, 30%, does a good job of removing noncorrelative components while minimizing amplitude reduction. A map of the percent of retained harmonics would parallel Figure 7, decreasing from 90% at degree 20 to 40% at degree 170.

[25] The phase angle of each degree and order is defined as

$$\zeta_{nm} = \tan^{-1}\left(-\frac{h_{nm}}{g_{nm}}\right) \quad (8)$$

The phase angle difference is related to the correlation between the components as follows.

$$\rho_{nm} = \cos(\zeta_{nm} - \zeta'_{nm}) \quad (9)$$

The Lowes-Mauersberger [*Lowes*, 1974] spatial power spectra is often used to characterize large-scale features of the solution. It is defined as the mean square amplitude of the magnetic field produced by harmonics of degree n, or formally,

$$R_n = (n+1)\sum_{m=0}^{n}\left[(g_n^m)^2 + (h_n^m)^2\right] \quad (10)$$

[26] The power spectra of the sequential and coestimation approaches (Figure 9) exhibit a significant difference in amplitude, ascribable to the regularization inherent in the coestimation approach. The two approaches exhibit very similar shapes, in contrast to the shape of the power spectrum of *Purucker* [2008].

[27] The difference between the shapes of the spectra is ascribable to the incorrect incorporation of the B_θ field into the *Purucker* [2008] model, described earlier, a deficiency that does not affect the location of the magnetic features, only their strength, as can be seen by comparing local features, such as in and around the Serenitatis impact basin (Figure 10). As a consequence, these new maps now supercede the maps of *Purucker* [2008].

[28] The lack of power at degrees 1–14 in all of the maps, and the low correlations between the sequential and coestimation approaches, suggest a critical change in lunar properties at about this degree. Degree 15 corresponds to a wavelength of 666 km on the Moon, and the power spectra

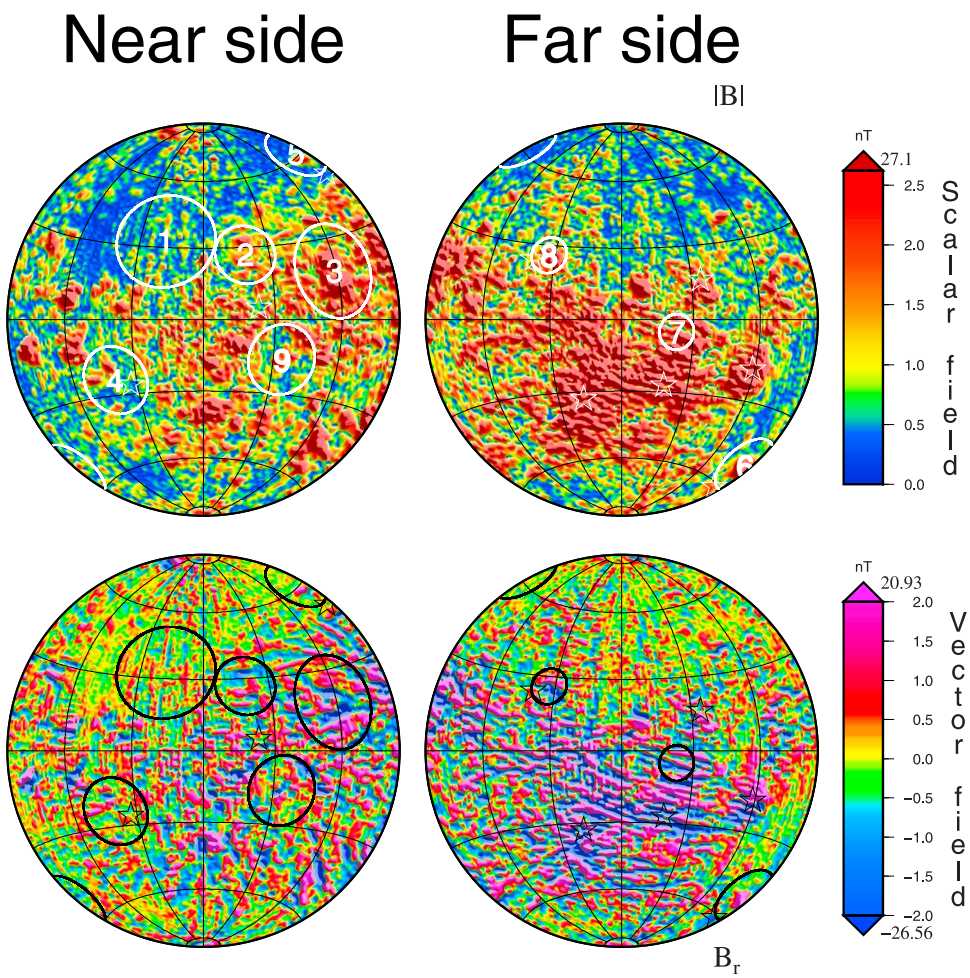

Figure 5. Global spherical harmonic model of the lunar magnetic field at an altitude of 30 km above the mean lunar radius made using the sequential (dipole) approach. (top) Scalar magnitude and (bottom) radial component fields. (left) Nearside maps and (right) farside maps. Illumination is from the north or east. Lambert equal area projection. Large impacts are shown as white circles and are numbered to correspond with their names: 1, Imbrium; 2, Serenitatis; 3, Crisium; 4, Humorum; 5, Humboldtianum; 6, Mendel-Rydberg; 7, Korolev; 8, Moscoviense; 9, Nectaris. The maximum and minimum values over the entire map are shown above and below the colored triangles which define the end points of the scale.

suggest that there are no magnetic features with wavelengths longer than this on the Moon. We suggest that this may relate to the Moon's impact history, and the large-scale demagnetizations that resulted from this impact history. For example, many of the Nectarian-aged craters, such as Serenitatis (Figure 10) have magnetic features associated with them, and many of the larger Nectarian craters are in the 600 km size range. These magnetic features are the largest-scale magnetic features on the Moon.

[29] Related to the spatial power spectra is the concept of horizontal spatial resolution, which can be shown to be [*Thébault et al.*, 2010] a function of degree n

$$\lambda = \frac{2\pi r}{\sqrt{n(n+1)}} \tag{11}$$

where r is the Moon's mean radius. Therefore our degree 170 solution corresponds to a full wavelength resolution of 64 km.

[30] A magnetization map of the resulting field is made assuming radially oriented magnetization directions, and as a consequence it looks similar to the B_r map (Figure 8). The magnetization map suggests magnetizations may locally exceed 0.1 to 0.2 A/m (Figure 11) in the lunar crust at the resolution of the survey (64 km), if the crust is as thick as 40 km.

[31] The ambiguities inherent in the magnetization inverse problem allow uniformly magnetized shells of any amplitude to be added to the magnetization solution, with no effect on the measured magnetic field outside of the shell [*Runcorn*, 1975]. This means that it is impossible to distinguish between some plausible geologic scenarios unless samples of the magnetized bodies are available. As an example, there are two plausible geologic scenarios which might be appropriate for the Moon in the South Polar Aitken region (Figure 3). The first interpretation posits oppositely magnetized bodies implaced adjacent to one another, and the second interpretation posits similarly magnetized bodies

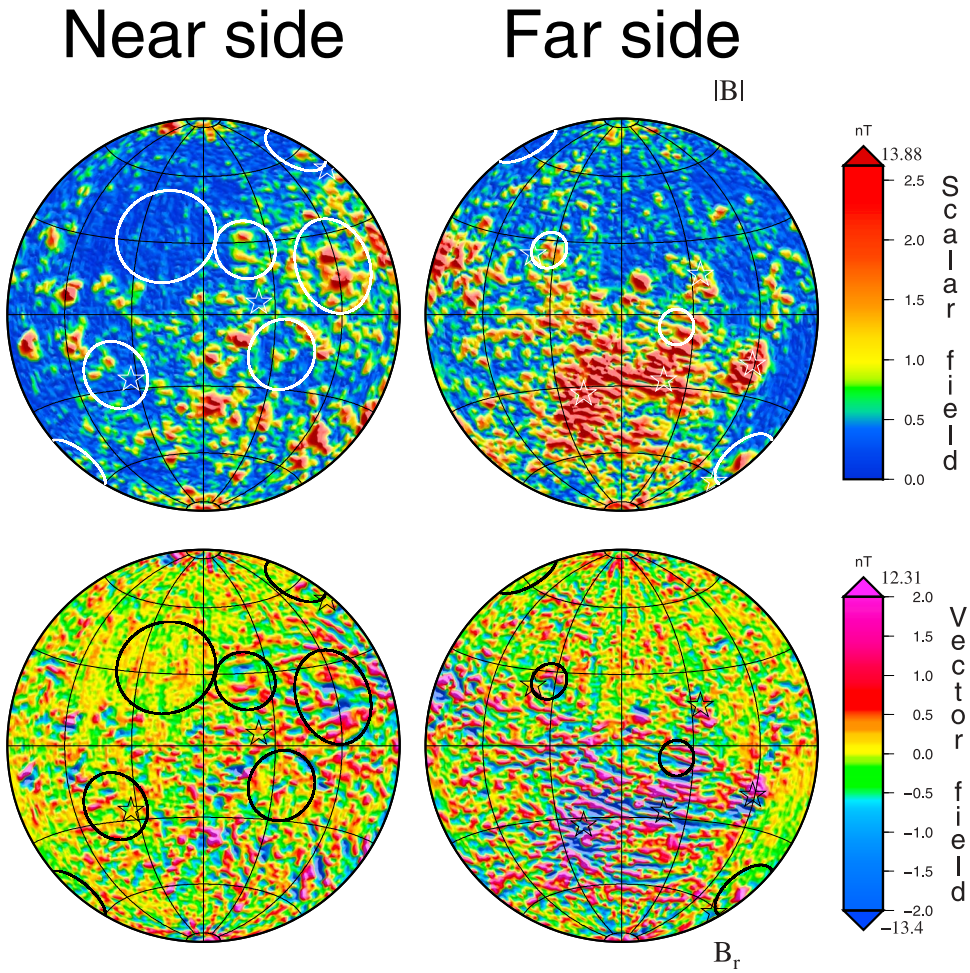

Figure 6. Map made using coestimation (harmonic for internal and uniform field for external) approach. See Figure 5 for further details. Antipodes of the basins are shown as unnumbered stars.

implaced at some larger distance apart, and with larger magnetizations. Similar ambiguities have been noted in the linear, strongly magnetic features of the Terra Sirenum region of Mars (M. Acuña, personal communication, 2006).

6. Discussion

[32] Comparison of the new magnetic field maps with the electron reflectometer map (Figure 12) of *Mitchell et al.* [2008] reveal little difference from previous assessments [*Purucker*, 2008]. The magnetic map made using the harmonic wave number correlation approach correlates with the electron reflectometer map with a linear correlation coefficient [*Press et al.*, 1992] of 0.60.

[33] As expected, the magnetic map also correlates strongly with the preliminary magnetic map of *Purucker* [2008] with a linear correlation coefficient of 0.9. The new magnetic map also correlates well with the new Kaguya magnetic map (Figure 13) of *Tsunakawa et al.* [2010]. Both utilized vector fluxgate magnetometers as the source of their observations. However, the Kaguya spacecraft was at much higher altitudes (100 km vs 30 km) for the first phase of its mission, and was a three-axis stabilized spacecraft in contrast to Lunar Prospector, which was spin stabilized. A map

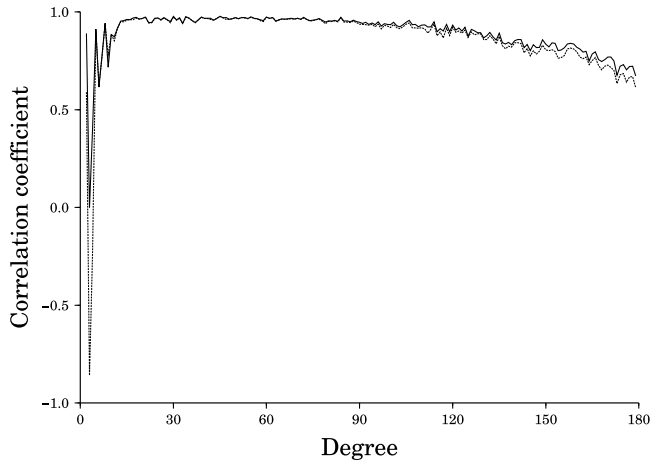

Figure 7. Correlation, by spherical harmonic degree, of the sequential and coestimation approaches. Dotted lines show the correlation before application of the harmonic wave number correlation technique; solid lines are after application of the technique.

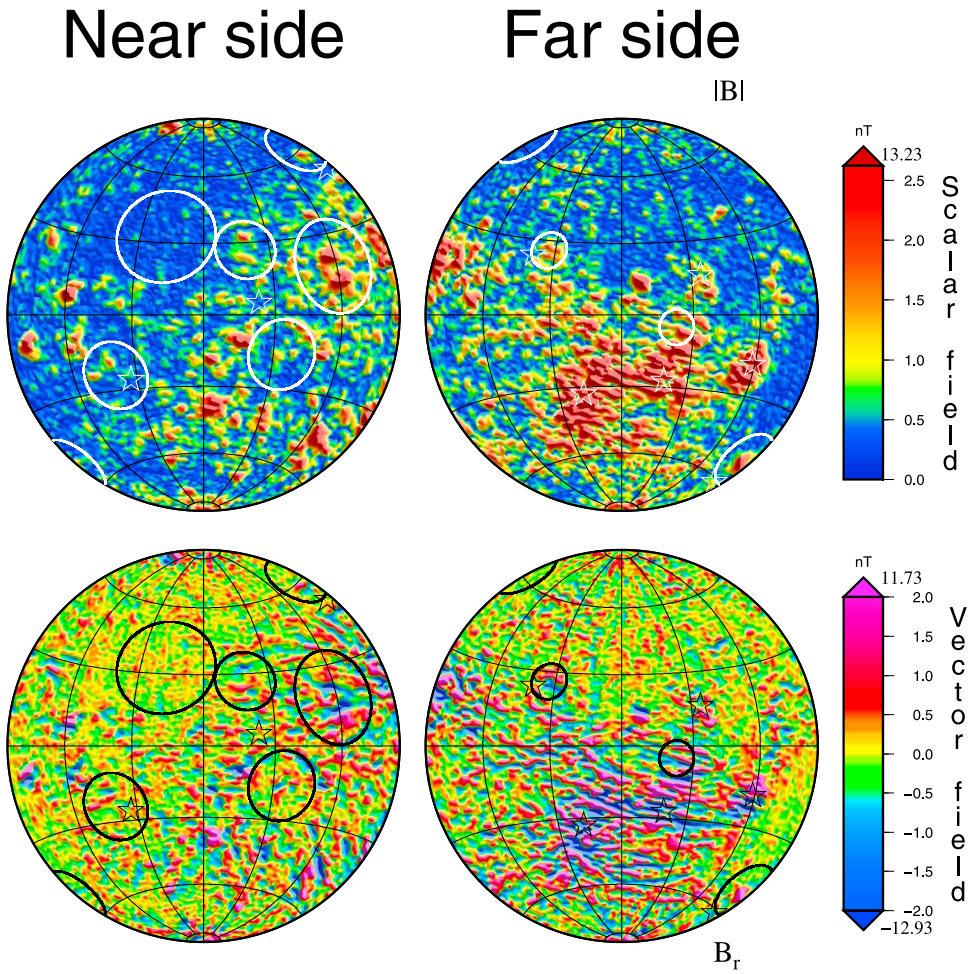

Figure 8. Combined radial and scalar magnetic field from sequential and coestimation approaches, retaining degrees with phases separated by less than 30°. Spherical harmonic degrees 1 through 170. Antipodes of the basins are shown as unnumbered stars. See Figure 5 for further details.

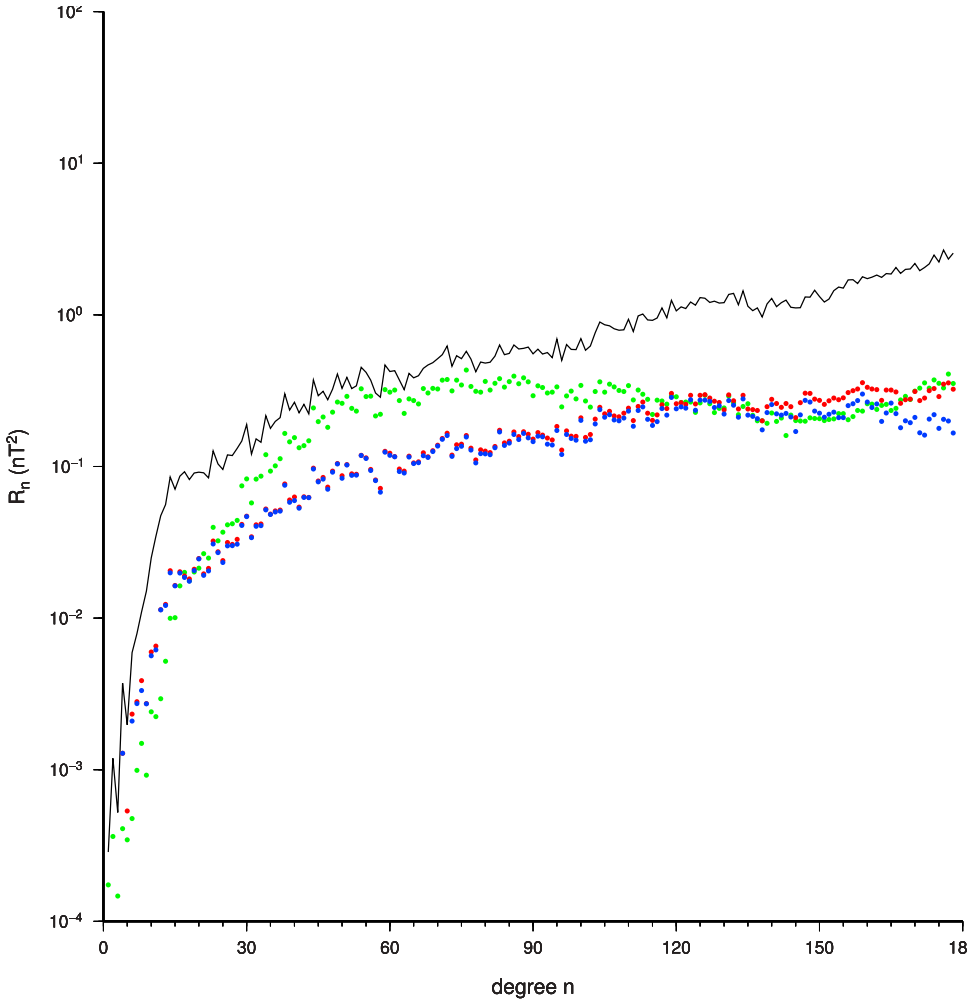

Figure 9. Lowes-Mauersberger [*Lowes*, 1974] power spectra of sequential (solid black line), coestimation (red dots), and correlative (blue dots) approaches and previous sequential approach (green dots) [*Purucker*, 2008]. R_n is the mean square amplitude of the magnetic field produced by harmonics of degree n.

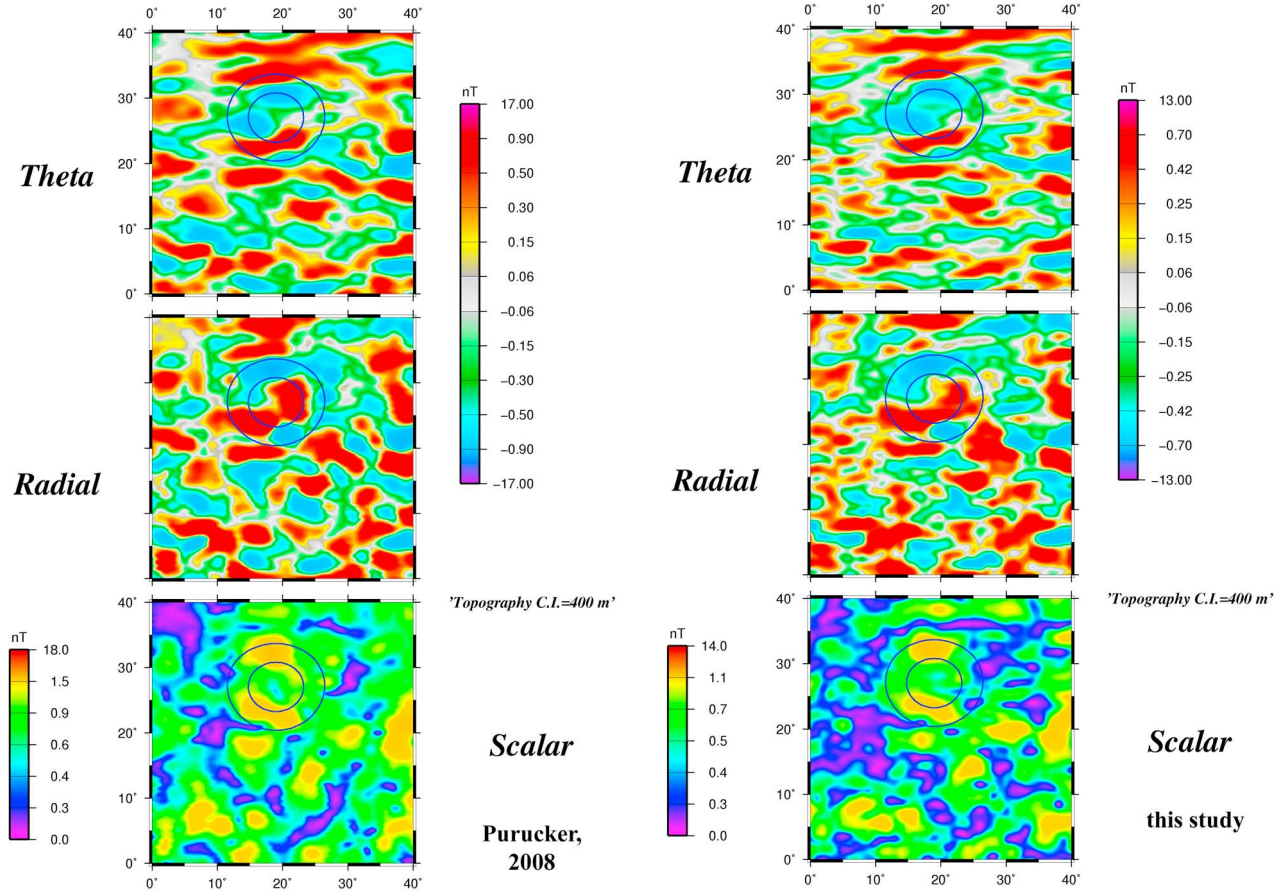

Figure 10. Magnitude, radial, and theta fields over the Serenitatis impact crater (inner and outer ring shown) in this study (harmonic correlation map) compared with the map of *Purucker* [2008]. Azimuthal equidistant projection.

of the radial magnetic fields at 30 km and 100 km reveal the presence of the WNW trending patterns over the South Polar Aitken basin region in both maps, although the pattern is considerably attenuated in the Kaguya map, because of its 100 km altitude. Upward comparison of our sequential and coestimation maps to 100 km altitude reveal virtually identical features in the Kaguya and Lunar Prospector maps (Figure 13). The linear correlation coefficients between the scalar maps at 100 km is 0.91. We also note that the amplitude of our upward continued coestimation map agrees most closely with the Kaguya map. The amplitudes from our sequential map are slightly higher than those seen in the Kaguya map. Detailed comparison awaits the analysis of the lower-altitude Kaguya data sets.

[34] The error levels of the two maps can be assessed by means of maps of the rejected components of the harmonic wave number correlation approach (Figure 14). These maps reveal that the errors are scattered about the surface, and are small.

[35] We expect that the maps will be utilized to further understanding of lunar tectonics (Figure 3), basins (Figure 10), swirls (Figure 2), and the nature of the primordial lunar field.

[36] We expect that future maps made using Lunar Prospector data may be able to increase the map resolution, at least locally. The ultimate limit is set by the spin averaging (9 km along track) of the Lunar Prospector data, which yields 3 observations per degree latitude. This corresponds to 540 field samples from pole to pole, which would theoretically [*Driscoll and Healy*, 1994] allow a degree and order 270 model to be developed. However, only 96%

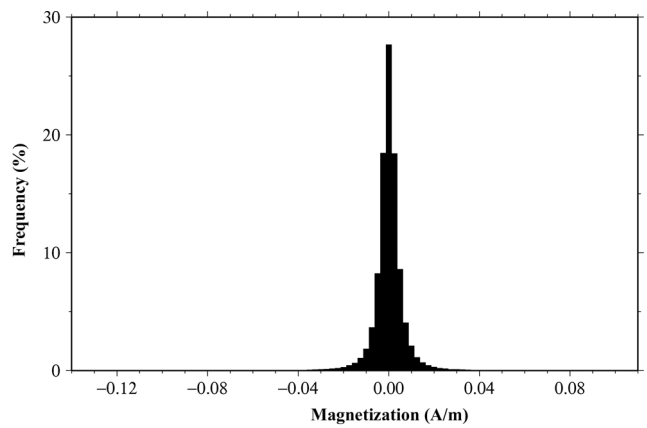

Figure 11. Histogram showing the distribution of magnetizations (range is −0.14 A/m to 0.10 A/m) calculated from the sequential model made using a space domain/conjugate gradient approach [*Purucker et al.*, 1996]. Magnetization values assume a 40 km thick crust.

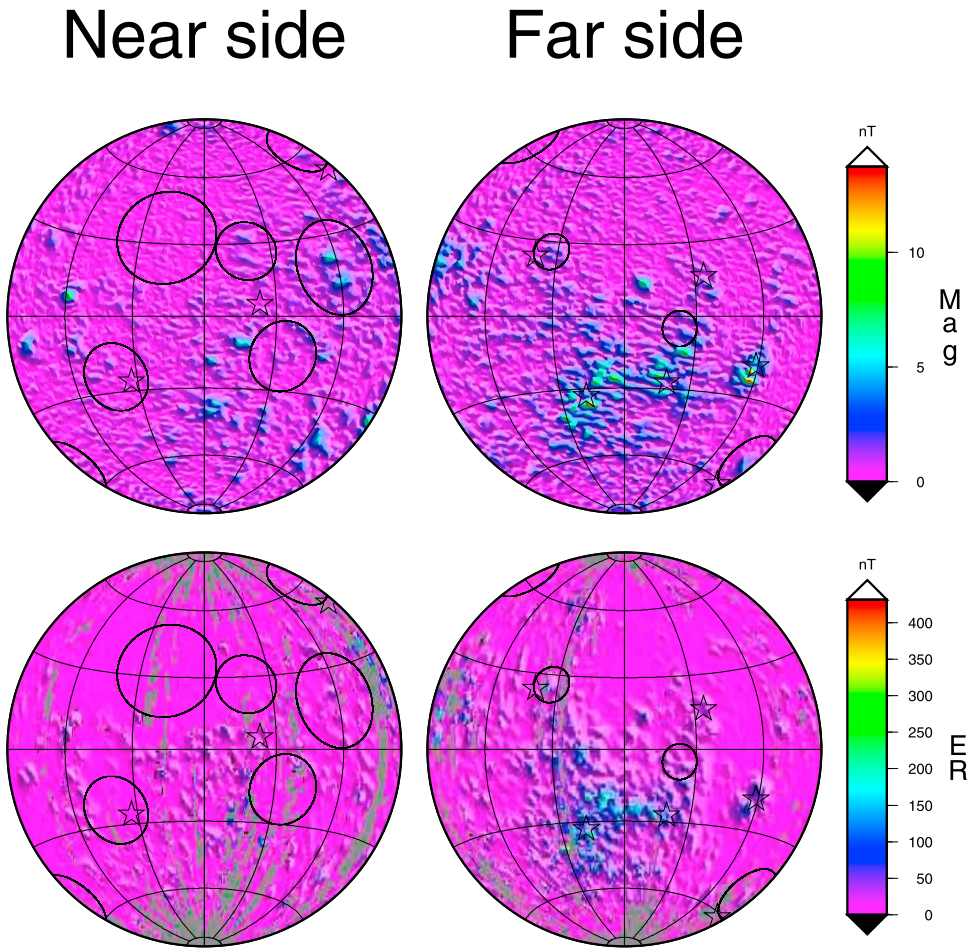

Figure 12. Magnitude of magnetic field measured by the Magnetometer (MAG) and Electron Reflectometer (ER) instruments onboard Lunar Prospector. See Figure 5 for further details.

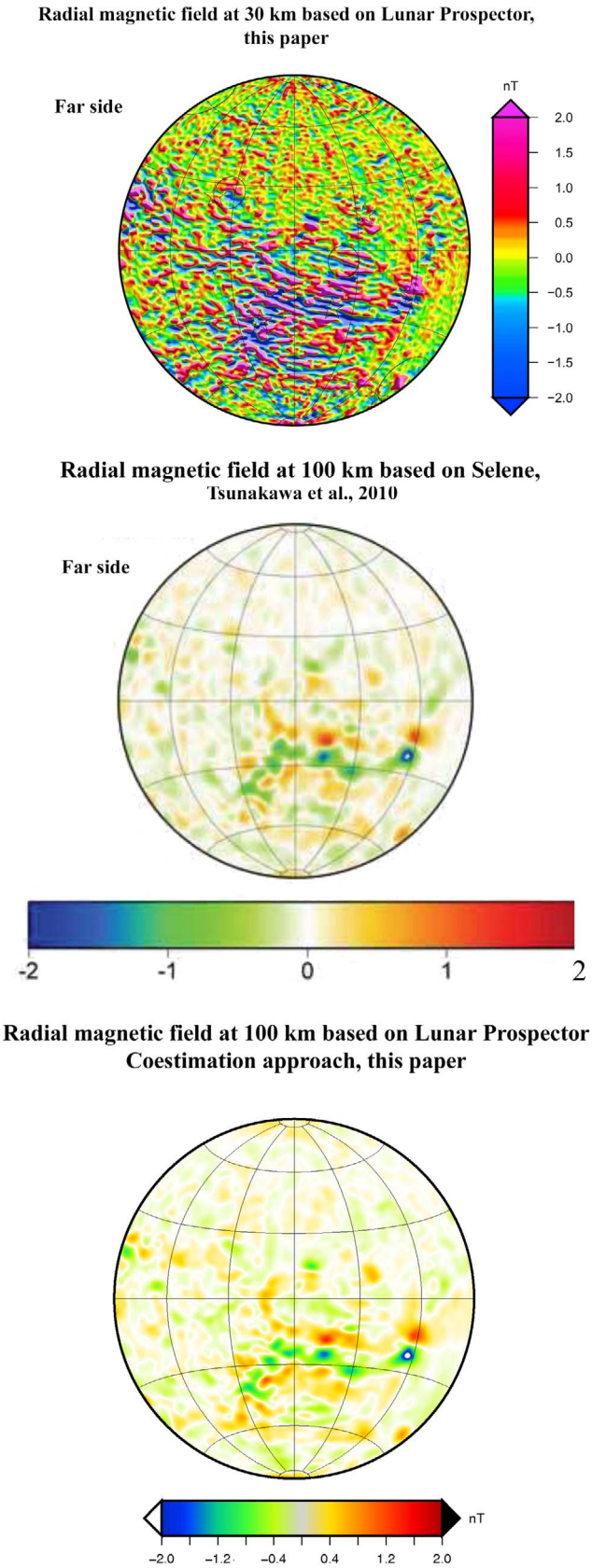

Figure 13. Comparison of the radial magnetic fields from Kaguya at 100 km altitude [*Tsunakawa et al.*, 2010] with those from our harmonic correlative model at 30 km and with our coestimation model upward continued to 100 km.

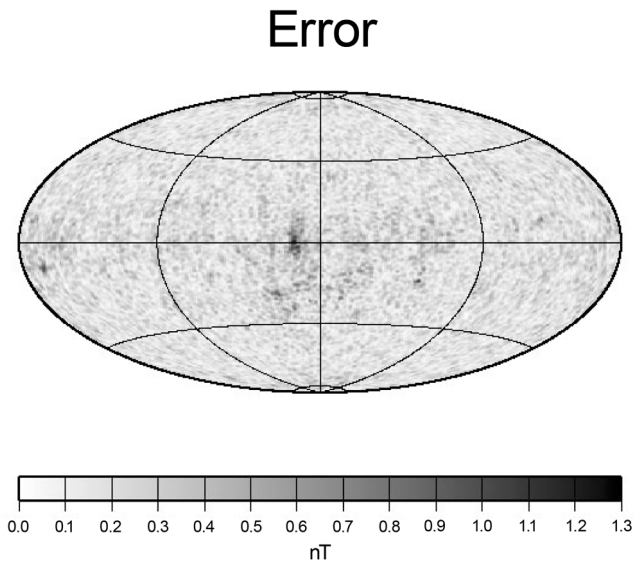

Figure 14. Magnitude of the rejected component of the harmonic map. Hammer projection extending from 0° to 360° Longitude.

of the 1/3rd by 2/3rd degree bins corresponding to a degree 270 model are filled, in contrast to more than 99% in the present model. However, there are still improvements to be made that would increase the fidelity of the maps. Future enhancements to internal lunar magnetic models certainly include more physically based models of the external magnetic field and particles environment, and inclusion of information on anisotropic errors in the Lunar Prospector measurements. Lunar Prospector was spin stabilized, and we expect that magnetic fields will be most accurately determined in the spin plane. Although this directional information is not included in the Level 1B data set, it might realistically be extracted from archived spacecraft data.

7. Conclusion

[37] This study presents the highest-resolution maps of the internal magnetic field of the Moon available to date. Magnetic fields with wavelengths in excess of 666 km are largely absent from the Moon, a consequence of its cratering history. Even higher-resolution maps of the internal magnetic field would allow for a much expanded understanding of the processes at work in the lunar interior and surface. While surface measurements would provide the highest resolution, they would also be the most expensive to obtain, and global coverage would be prohibitively expensive. A possible approach to providing higher resolution would involve magnetic gradiometry from two or more satellites flying nearby, or in a string of pearls configuration. Such a

configuration will be employed to map the Earth's crustal field by the upcoming Swarm satellites [*Friis-Christensen et al.*, 2009]. The digital data (models and grids) presented in this manuscript can be obtained from http://core2.gsfc.nasa.gov/research/purucker/moon_2010.

[38] **Acknowledgments.** We would like to acknowledge the Lunar Prospector team and especially the late Mario Acuña for the collection of this data set. M. Wieczorek, J. Head, N. Olsen, J. Halekas, D. Clark, V. Lesur, T. Sabaka, H. Tsunakawa, I. Garrick-Bethell, C. Russell, K. Whaler, and L. Hood provided valuable comments, data sets, or codes. We thank H. Tsunakawa for the Selene global magnetic model. M. Mandea provided an uninterrupted time for writing at Boiscommun, and B. Langlais, R. Lillis, D. Blewett, J. Slavin, and H. Frey were a source of stimulating discussions on related topics. A. Isac provided assistance with the figures. M. Purucker and J. Nicholas were supported by a NASA Discovery Data Analysis Program (DDAP) contract. GMT [*Wessel and Smith*, 1998] was used for the graphics and some analysis. SHTOOLS, by M. Wieczorek (IPGP), was used to implement the Driscoll and Healy sampling theorem [*Driscoll and Healy*, 1994]. We thank an anonymous reviewer and the Editor for improvements to the manuscript.

References

Binder, A. (1998), Lunar Prospector overview, *Science*, *281*, 1475–1476.

Driscoll, J. R., and D. M. Healy (1994), Computing Fourier transforms and convolutions on the 2-sphere, *Adv. Appl. Math.*, *15*, 202–250.

Dyment, J., and J. Arkani-Hamed (1998), Equivalent source dipoles revisited, *Geophys. Res. Lett.*, *25*, 2003–2006.

Friis-Christensen, E., H. Lühr, G. Hulot, R. Haagmans, and M. Purucker (2009), Geomagnetic research from space, *Eos Trans. AGU*, *90*(25), 213–214.

Fuller, M. (1998), Lunar magnetism-a retrospective view of the Apollo sample magnetic studies, *Phys. Chem. Earth*, *23*, 725–735.

Garrick-Bethell, I., B. Weiss, D. L. Shuster, and J. Buz (2009), Early lunar magnetism, *Science*, *323*, 356–359.

Halekas, J. S., D. L. Mitchell, R. P. Lin, S. Frey, M. H. Acuña, and A. B. Binder (2001), Mapping of lunar crustal magnetic fields using lunar prospector electron reflectometer data, *J. Geophys. Res.*, *106*, 27,841–27,852.

Hood, L., and N. Artemieva (2008), Antipodal effects of lunar basin-forming impacts: Initial 3-D simulations and comparisons with observations, *Icarus*, *193*, 485–502.

Hood, L. L., A. Zakharian, J. Halekas, D. L. Mitchell, R. P. Lin, M. H. Acuña, and A. B. Binder (2001), Initial mapping and interpretation of lunar crustal magnetic anomalies using Lunar Prospector magnetometer data, *J. Geophys. Res.*, *106*, 27,825–27,839.

Langel, R. A. (1987), The main geomagnetic field, in *Geomagnetism*, vol. 1, edited by J. A. Jacobs, pp. 249–512, Academic, London.

Langel, R. A., and W. J. Hinze (1998), *The Magnetic Field of the Earth's Lithosphere: The Satellite Perspective*, Cambridge Univ. Press, New York.

Lowes, F. J. (1974), Spatial power spectrum of the main geomagnetic field, and extrapolation to the core, *Geophys. J. R. Astron. Soc.*, *36*, 717–730.

Matsushima, M., et al. (2010), Magnetic cleanliness program under control of electromagnetic compatibility for the SELENE (Kaguya) spacecraft, *Space Sci. Rev.*, doi:10.1007/s11214-010-9655-x, in press.

Mitchell, D., J. Halekas, R. Lin, S. Frey, L. Hood, M. Acuña, and A. Binder (2008), Global mapping of Lunar crustal magnetic fields by Lunar Prospector, *Icarus*, *194*, 401–409.

Nicholas, J., M. Purucker, and T. Sabaka (2007), Age spot or youthful marking: Origin of Reiner Gamma, *Geophys. Res. Lett.*, *34*, L02205, doi:10.1029/2006GL027794.

Press, W., S. Vetterling, and W. Flannery (1992), *The Art of Scientific Computing*, 2nd ed., Cambridge Univ. Press, New York.

Purucker, M. (2008), A global model of the internal magnetic field of the moon based on lunar prospector magnetometer observations, *Icarus*, *197*, 19–23.

Purucker, M., T. Sabaka, and R. Langel (1996), Conjugate gradient analysis: A new tool for studying satellite magnetic data sets, *Geophys. Res. Lett.*, *23*, 507–510.

Richmond, N., and L. Hood (2008), A preliminary global map of the vector lunar crustal magnetic field based on Lunar Prospector magnetometer data, *J. Geophys. Res.*, *113*, E02010, doi:10.1029/2007JE002933.

Runcorn, S. (1975), On the interpretation of lunar magnetism, *Phys. Earth Planet. Inter.*, *10*, 327–335.

Shimizu, H., F. Takahashi, N. Horii, A. Matsuoka, M. Matsushima, H. Shibuya, and H. Tsunakawa (2008), Ground calibration of the high-sensitivity SELENE lunar magnetometer LMAG, *Earth Planets Space*, *60*, 353–363.

Takahashi, F., H. Shimizu, M. Matsushima, H. Shibuya, A. Matsuoka, S. Nakazawa, Y. Iijima, H. Otake, and H. Tsunakawa (2009), In-orbit calibration of the lunar magnetometer onboard SELENE (KAGUYA), *Earth Planets Space*, *61*, 1269–1274.

Thébault, E., M. Purucker, K. Whaler, B. Langlais, and T. Sabaka (2010), The magnetic field of the Earth's lithosphere, *Space Sci. Rev.*, doi:10.1007/s11214-010-9667-6, in press.

Toyoshima, M., H. Shibuya, M. Matsushima, H. Shimizu, and H. Tsunakawa (2008), Equivalent source mapping of the linuar crustal magnetic field using ABIC, *Earth Planets Space*, *60*, 365–373.

Tsunakawa, H., H. Shibuya, F. Takahashi, H. Shimizu, M. Matsushima, A. Matsuoka, S. Nakazawa, H. Otake, and Y. Iijima (2010), Lunar magnetic field observation and initial global mapping of lunar magnetic anomalies by MAP-LMAG onboard SELENE (kaguya), *Space Sci. Rev.*, doi:10.1007/s11214-010-9652-0, in press.

Wessel, P., and W. Smith (1998), New improved version of Generic mapping tools released, *Eos Trans. AGU*, *79*, 579.

J. B. Nicholas and M. E. Purucker, Raytheon at Planetary Geodynamics Laboratory, Code 698, Goddard Space Flight Center, Greenbelt, MD 20771, USA.